

Research Article

Microwave Synthesis of MCM-41 and Its Application in CO₂ Absorption by Nanofluids

Shang-Yuan Cheng , You-Zhi Liu , and Gui-Sheng Qi

Shanxi Province Key Laboratory of Hige-Oriented Chemical Engineering, North University of China, Taiyuan 030051, China

Correspondence should be addressed to You-Zhi Liu; lyzzhongxin@126.com

Received 21 December 2019; Revised 10 February 2020; Accepted 20 February 2020; Published 28 April 2020

Academic Editor: Fabien Grasset

Copyright © 2020 Shang-Yuan Cheng et al. This is an open access article distributed under the Creative Commons Attribution License, which permits unrestricted use, distribution, and reproduction in any medium, provided the original work is properly cited.

Microwave synthesis method is a green chemical process with mild reaction conditions, fast reaction, and low energy consumption. In this work, an order mesoporous silica material MCM-41 was synthesized by microwave technology. Functionalized MCM-41 was prepared by wet impregnation with polyethyleneimine (PEI). XRD, SEM, TEM, DLS, N₂ adsorption-desorption, FTIR, and TG were used to characterize the physicochemical properties of samples. Furthermore, CO₂ absorption performance in water in the presence of uncalcined MCM-41 and PEI-MCM-41 nanoparticles was evaluated. In addition, the mechanisms of enhanced absorption were also elaborated. The experimental results indicated that the optimum conditions for preparation of MCM-41 were the microwave time of 15 min, microwave temperature of 100°C, and microwave power of 200 W. Under this condition, MCM-41 with narrow particle size distribution, average diameter of 50 nm, and S_{BET} of 1210.3 m²g⁻¹ was obtained. The enhancement effect of PEI-MCM-41 nanoparticles was more obvious than that of uncalcined MCM-41. PEI-MCM-41 as a promoter not only increased the CO₂ diffusion rate but also enhanced the adsorption capacity due to the fact that it owns more active sites that may react with CO₂. The CO₂ absorption improvement of PEI-MCM-41 (0.1 wt%)/H₂O was 25.35% higher than that of water.

1. Introduction

With the intensification of the industrialization process in the world, the burning of fossil fuels is increasing, which rapidly increases the content of greenhouse gases in the atmosphere. Greenhouse gases will directly contribute to global warming, which may lead to a series of serious consequences such as rising sea levels, ocean acidification, dramatic climate change, and ecosystem disorder [1]. Among these gases, CO₂ contributes about 60% to global warming [2]. According to the Global Carbon Project (GCP), global annual CO₂ emissions reached a record high of 37.1 billion tons by 2018 [3]. Therefore, carbon capture and storage technology (CCS) is the focus of current researches [4–6]. CO₂ capture is the first step of CCS, mainly including liquid phase absorption method [7–9], solid phase adsorption method [10–12], cryogenic method [13–15], and membrane separation method [16–18]. Among the different methods, liquid phase absorption is widely used in CO₂ absorption. In this process, the

gas-liquid mass transfer effect plays an important role. Further strengthening the mass transfer between gas and liquid can not only improve the CO₂ removal rate but also reduce operating costs and equipment volume.

Many studies have found that adding nanoparticles to the solvents to obtain nanofluids can effectively improve the gas-liquid mass transfer rate and enhance the absorption process [19–21]. It is a new type of gas-liquid mass transfer enhancement technology that has emerged in recent years. Initially, nanofluids have a wide range of applications in the field of heat transfer due to its ability to reduce heat transfer resistance and enhance the heat transfer coefficient [22, 23]. Due to the similarity between mass transfer and heat transfer, more and more scholars have realized that nanofluids also have great application potential in enhancing mass transfer. Li and Zou [24] synthesized functionalized β-CD-TiO₂-Ag nanoparticles and added them in ionic liquids (IL) to test the desulfurization of simulation the gasoline. The results showed that the order of desulfurization efficiency was pure



FIGURE 1: Schematic diagram of synthesis of MCM-41 by the microwave synthesis method.

ILs<math>\text{TiO}_2/\text{ILs}<\mathit{\beta}<math>\text{CD-TiO}_2-Ag/ILs. The sulfur content of the simulated oil in the sample of β -CD-TiO₂-Ag/ILs (0.5 vol%) was 0 ppm, while that of TiO₂/ILs (0.5 vol%) was 425.62 ppm.

Mesoporous nanomaterial such as MCM-41 (Mobil Composition of Matter No. 41) is a suitable nanoparticle additive due to its uniform pore size, large specific surface area, and easy modification of hydroxyl groups. Amine-functionalized adsorbents can increase the ability to adsorb CO₂. However, MCM-41 is usually synthesized by a conventional hydrothermal method, which consumes energy and time [25]. In order to reduce the energy consumption of MCM-41 synthesis, microwave is applied as an alternative heat source. The microwave synthesis has the characteristics of rapid heating, uniformity, and strong penetrability, which can promote the effective combination of silicon species and surfactants at the interface and rapidly nucleate during crystallization. Therefore, this method can greatly shorten the crystallization time, reduce the energy consumption, and obtain uniform fine particles.

Of note, the CO₂ absorption enhanced by MCM-41 nanoparticles has rarely been reported. Among amine compounds, branched polyethyleneimine (PEI) can effectively bind CO₂ due to its high amine density and accessible primary amine sites at the chain ends. In this work, MCM-41 was synthesized by microwave technology and then modified with PEI. The effects of different microwave conditions on MCM-41 were elucidated minutely in this paper to obtain the optimum conditions. Furthermore, CO₂ absorption performance by MCM-41 and PEI-MCM-41 nanoparticles in water was evaluated in the bubbling reactor. In addition, the mechanism for the enhancement of mass transfer was also discussed in detail.

2. Experimental

2.1. Materials. The following chemical reagents were used in the syntheses: tetraethyl orthosilicate (TEOS, 40% in water), cetyltrimethylammonium bromide (CTAB), sodium hydroxide (NaOH), polyethyleneimine (PEI, average molecular weight of 600), and anhydrous methanol. All chemicals were used as received without any further purification.

2.2. Synthesis of MCM-41 by Microwave Synthesis Method.

The synthesis of MCM-41 was based on the method reported by Misran et al. [26]. Figure 1 illustrates the procedure for the synthesis of MCM-41. Primarily, 1.275 g CTAB was dissolved in 100 ml deionized water at room temperature. Under vigorous stirring, 2.708 g TEOS was tardily added to the solution and the mixed solution was incessantly stirred for 2 h. The pH of the mixture was adjusted to 10.8 by 2 M NaOH solution. After that, the obtained gel was placed in an 80 ml microwave vessel and heated under certain conditions. The resulted white solid was centrifuged at high speed, washed with distilled water, dried in air overnight, and calcined at 500°C for 5 h. The prepared samples were labeled as WH-XY (X indicates the factor affecting microwave synthesis, and Y represents the specific value of the factor). For example, WH-T100 denotes the MCM-41 sample synthesized under microwave temperature at 100°C.

2.3. Synthesis of PEI-MCM-41. Functionalized MCM-41 was prepared by wet impregnation adapted from other research groups. Accordingly, 0.43 g of PEI was dissolved in 8 g of methanol under mechanically stirring for 15 min. Then, 1 g of uncalcined MCM-41 powder was added into the mixture under stirring for 24 h. The reaction process was protected by nitrogen. The functionalized MCM-41 was dried at 70°C in a vacuum oven for 12 h. Subsequently, the resulting sample was identified as PEI-MCM-41.

2.4. Preparation of Nanofluids. Nanofluids were prepared by a two-step method. Primarily, a certain amount of nanoparticles (uncalcined MCM-41 or PEI-MCM-41) was added to distilled water and mechanically stirred for 15 min. Then, the suspension was dispersed in an ultrasonic bath at 30°C for 60 min. Batch-type vibration method with a six-second interval after vibration for four seconds was adopted to avoid dramatical rise of solution temperature. Zeta potential was used to quantify the stability of colloid dispersion. It is widely accepted that nanofluids with zeta potential (positive or negative) of more than 25 mV are physically stable.

2.5. Experimental Setup of CO₂ Absorption by Nanofluids.

Figure 2 shows the schematic diagram of the experimental

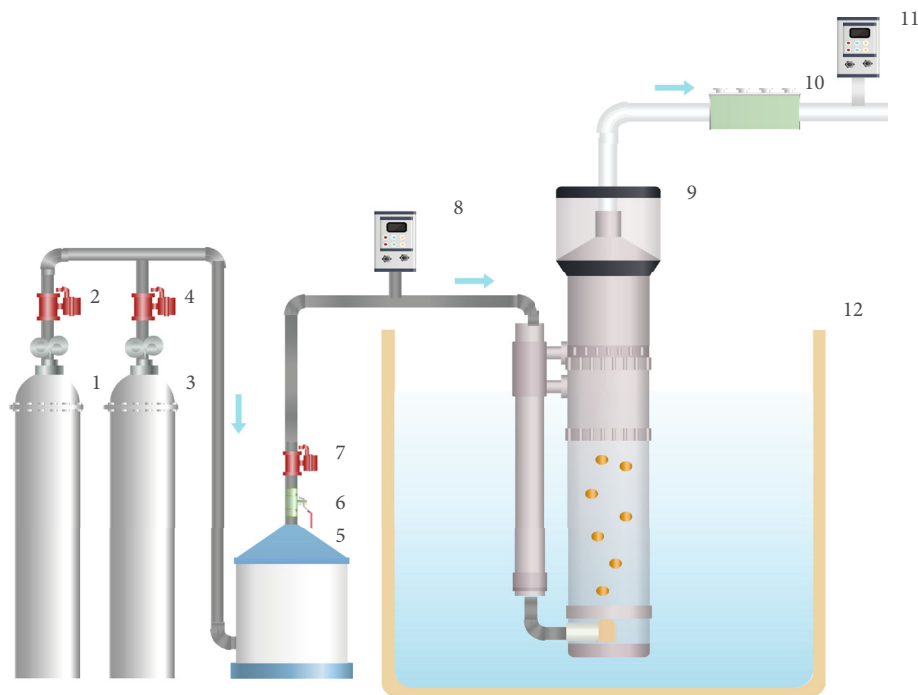


FIGURE 2: Schematic diagram of CO₂ absorption experimental setup: 1, CO₂ cylinder; 3, N₂ cylinder; 2, 4, and 7, gas flow meter; 5, buffer tank; 6, valve; 8 and 11, CO₂ analyzer; 9, bubble reactor; 10, dry tube; 12, water bath.

setup for CO₂ absorption process. The bubbling reactor made of plexiglass has a height of 257 mm and a diameter of 180 mm. And a gas diffuser (10 μm pores) was mounted at the bottom of the reactor. The temperature was controlled by water bath. In all experiments, the bubble reactor was filled with 180 ml of the absorbents. The initial CO₂ concentration was maintained at 10 vol% while the volumetric flow rate was fixed at 100 ml/min. After absorption, the outlet gas entered a dry tube to remove the water vapor. The CO₂ concentration in the outlet gas stream was measured every 3 s over a period of 600 s by the online infrared flue gas analyzer (GXH-3011N). Obviously, the amount of nitrogen is constant before and after CO₂ absorption (Equation (1)).

$$Q_{\text{in}}(1 - c_{\text{in}}) = Q_{\text{out}}(1 - c_{\text{out}}), \quad (1)$$

where Q_{in} and Q_{out} are the inlet and outlet gas volume flow rate and c_{in} and c_{out} are the initial and residual CO₂ volume fractions. The real-time absorbed CO₂ volume per 3 s can be calculated by Equation (2).

$$\Delta V_{\text{CO}_2} = \Delta Q = Q_{\text{in}} - Q_{\text{out}} \frac{c_{\text{in}} - c_{\text{out}}}{1 - c_{\text{out}}}. \quad (2)$$

The total volume of CO₂ absorbed within 600 s is the summation of every real-time absorbed CO₂ volume (Equation (3)).

$$V_{\text{CO}_2} = \sum_{t=1}^{600} \Delta V_{\text{CO}_2}. \quad (3)$$

The enhancement percentage was calculated by the following equation:

$$\text{Enhancement}(\%) = \frac{V_{\text{absorbed CO}_2 \text{ by nanofluid}} - V_{\text{absorbed CO}_2 \text{ by water}}}{V_{\text{absorbed CO}_2 \text{ by water}}}. \quad (4)$$

2.6. Characterization. The phase analysis of samples was verified using powder X-ray diffraction (XRD, D8 ADVANCE A25) with Cu K α radiation (1.5418 Å) over the scanning range $2\theta = 1^\circ - 8^\circ$ for small-angle XRD. Fourier-transform infrared spectroscopy (FTIR) spectra of samples were obtained by using Spectrum Two. Dynamic light scattering (DLS, Zetasizer Nano ZS) was adopted to estimate the particle size distribution of samples and the stability of nanofluids. Transmission electron microscopy (TEM, JSM-7900F) and scanning electron microscopy (SEM, JEOL JEM-6490LV) were used to study the structure, size, and morphology of the samples. Nitrogen adsorption-desorption isotherms were determined in a Micromeritics Tristar-3020 porosimeter. Textural properties were measured using BET and BJH methods. The samples were degassed at 200°C for 6 h before the surface area measurements. The thermal stability and the amount of amine loading of samples were determined by a STA449F3 thermogravimetric analyzer.

3. Results and Discussion

3.1. Effect of Different Microwave Conditions. The small-angle XRD patterns of samples under different microwave conditions are shown in Figure 3. All samples showed a

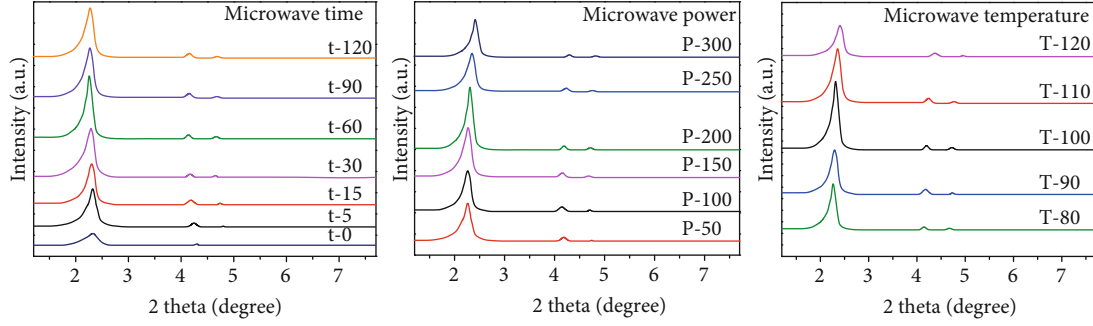


FIGURE 3: The small-angle XRD patterns of samples obtained under different microwave conditions.

well-defined diffraction peak around $2\theta = 2.3^\circ$ and two weak peaks at a slightly larger diffraction angle. They accordingly correspond to the (100), (110), and (200) characteristic diffraction peaks of a hexagonal unit cell [27]. The patterns illustrated the reflection of a typical MCM-41 type material. Furthermore, the (100) diffraction peak indicates that the sample has a hexagonal pore structure, and the (110) and (200) diffraction peaks indicate that the pores are long-range ordered [28]. With the increase of microwave power, temperature, and time, the diffraction peak intensity was correspondingly enhanced, and the phenomenon of offset occurred. This indicated that different synthesis conditions had effects on the mesoporous structure. In agreement with Kamarudin et al.'s results [29], Ergün et al. [30] also observed the phenomenon of diffraction peak deviation. According to the Bragg law (Formula (5)), the (100) interplanar spacing (d_{100}) could be calculated. The lattice parameter (a_0) representing the distance between centers of two adjacent pores was evaluated from Formula (6) [31]. The corresponding pore wall thickness (δ) was calculated by Formula (7) [32]. The calculation results are listed in Table 1. It can be seen that the pore wall thickness was thinner when microwave power and temperature were larger. The pore wall thickness increases first and then decreases with the increase of microwave time. The main reason is that the thickness of the pore wall is highly dependent on microwave energy. Under high power and temperature conditions, the reaction rate is fast. So the wall condensation is rapid, resulting in thin pore wall. The shorter microwave time is not enough to trigger the formation of an ordered structure. Continuous microwave action promotes the growth of the silicon skeleton, improves the order of the skeleton, and makes the formed pore walls denser. But too long microwave time results in decomposition of the already formed structure. This behavior is common for the conventional hydrothermal method.

$$d_{100} = \frac{\lambda}{2 \sin \theta}, \quad (5)$$

$$a = \frac{2d_{100}}{\sqrt{3}}, \quad (6)$$

$$\delta = a - 0.95D_{\text{pore}}. \quad (7)$$

Figure 4 shows the nitrogen adsorption-desorption isotherms of samples. The curves of the sample prepared without microwave heating exhibited a type II isotherm with the lowest specific surface area (Figure 4 (t0)). The nitrogen adsorption-desorption isotherms of other samples were similar in shape. According to the IUPA classification, the isotherms had a typical IV curve, which is a characteristic shape for mesoporous materials [33]. Three well-defined stages were identified as follows: (1) at a low relative pressure, nitrogen is gradually increased with monolayer/multilayer adsorption on the pore walls; (2) under relative pressure from 0.25 to 0.4, the amount of nitrogen adsorption rises sharply due to the capillary condensation of nitrogen in the mesoporous structure; and (3) the presence of a narrow hysteresis loop when the relative pressure is greater than 0.4 indicates that the samples are mesoporous materials with uniform cylindrical channels. At higher relative pressure, multilayer adsorption occurs on the external surface of the samples. It can be seen from Table 1 that as microwave power increases, S_{BET} , D , and V all show a trend of first increasing and then decreasing. The best sample was obtained at the microwave power of 200 W. This would be due to that the increase of microwave power enhanced the hydration degree of CTAB chain to some extent and its interaction with the silicon species in solution. At the same time, the hydrolysis and polymerization rate of TEOS was accelerated to form MCM-41 with a better pore structure [29]. However, since the microwave heating process was instantaneous, excessive microwave power might cause local overheating, resulting in differences in S_{BET} and V . With the increase of microwave temperature, S_{BET} , D , and V all increased first and then decreased. The best sample was obtained when microwave temperature was 100°C . The key step in achieving rapid synthesis of mesoporous silica is to control the condensation of silica to form Si-O-Si siloxane bridges. It is a highly active kinetic process which is primarily affected by temperature [30]. At low temperatures, inferior condensation rate was not conducive to the formation of stable silicate frameworks. Increasing the microwave temperature increased the collision frequency of reactants. It accelerated interface self-assembly and condensation process, which can easily form an ordered structure. However, if the temperature was too high, the formed structure would be partially decomposed. The formation of "hot spots" during a shorter radiation time did not

TABLE 1: Properties of MCM-41 synthesized at different microwave conditions.

Sample	Different parameters Factor	Value	$S_{\text{BET}}^{\text{a}}$ (m^2g^{-1})	V^{b} (cm^3g^{-1})	D^{c} (nm)	d_{100} (\AA)	a_0 (\AA)	δ (\AA)
WH-t0		0	518.1	0.663	3.027	37.77	43.61	—
WH-t5	Microwave time (min)	5	1158.3	1.069	3.815	38.11	44.01	7.77
WH-t15		15	1210.3	1.224	3.825	38.41	44.35	8.01
WH-t30		30	1115.6	1.088	3.821	38.75	44.74	8.44
WH-t60		60	1102.0	1.149	3.815	39.26	45.33	9.09
WH-t90		90	1095.1	1.199	3.824	39.26	45.33	9.00
WH-t120		120	1053.5	1.146	3.815	38.92	44.94	8.70
WH-T80		Microwave temperature ($^{\circ}\text{C}$)	80	1164.7	0.976	3.820	38.99	45.02
WH-T90	90		1180.1	0.991	3.823	38.61	44.58	8.26
WH-T100	100		1210.3	1.224	3.825	38.41	44.35	8.01
WH-T110	110		1200.3	1.214	3.824	37.55	43.36	7.03
WH-T120	120		903.3	0.939	3.813	36.72	42.40	6.18
WH-P50	Microwave power (W)	50	928.1	0.954	3.806	39.00	45.03	8.87
WH-P100		100	997.1	0.942	3.812	39.16	45.22	9.01
WH-P150		150	1188.4	1.195	3.821	38.76	44.76	8.46
WH-P200		200	1210.3	1.224	3.825	38.41	44.35	8.01
WH-P250		250	1182.3	1.222	3.814	37.55	43.36	7.13
WH-P300		300	937.2	0.960	3.805	36.58	42.34	6.19

^aBET method. ^b t -plot method. ^cMean pore width was determined using the BJH method.

provide uniform heating and was not sufficient to induce a better ordered structure. Nevertheless, sustained microwave action may cause a metastable precursor to collapse into denser amorphous phases in the reaction solution. The optimum microwave time was 15 min. Compared to the traditional hydrothermal synthesis method (1~3 days) [34], the synthesis time is greatly shortened.

The effect of operating parameters on the particle size distribution of samples is shown in Figure 5. When the microwave time, temperature, and power were 15 min, 100 $^{\circ}\text{C}$, and 200 W, respectively, the particle size distribution of the sample was the narrowest and the peak particle size was the smallest. The particle size of samples depends on the nucleation rate and growth rate [29]. Increasing microwave power and temperature will accelerate the crystallization rate and nucleation rate, which can easily produce samples with small particle size and uniform distribution. However, as the microwave time prolongs, the aggregation of silicon species on the surface of the coated micelle increases, the sample continues to grow, and the particle size gradually becomes larger. It means that appropriate microwave radiation can facilitate forming small particles.

Therefore, the optimum parameters for synthesis of MCM-41 through microwave can be determined by the textural properties and the particle size distribution. It is found that the suitable synthesis can be achieved at a microwave time of 15 min, microwave temperature of 100 $^{\circ}\text{C}$, and microwave power of 200 W. As evident from the SEM image (Figures 6(a) and 6(b)), the sample synthesized by the microwave synthesis method has a uniform morphology and shows a spheroidal shape with the average particle size about 50 nm. The distribution measured through the DLS method

was larger than the particle size measured by SEM. This would be attributed to the fact that the water molecules are on the surface of the nanoparticles [35]. As can be seen from the TEM image (Figures 6(c) and 6(d)), the WH-T100 sample has highly ordered regular channels in the vertical direction. This is the long-range structure of a MCM-41 one-dimensional channel. The mesoporous channel section can be seen as a regular hexagon in the direction of the channel. It is further proved that MCM-41 prepared by microwave has a good mesoporous structure.

Overall, the microwave synthesis method can rapidly prepare MCM-41 with large specific surface area ($1210.3\text{ m}^2\text{g}^{-1}$), small particle size (50 nm), and uniform distribution. The mesoscopic structure of MCM-41 is the result of cooperation and coassembly of inorganic species and organic surfactant molecules, that is, the “cooperative formation mechanism.” As shown in Figure 7, during the synthesis of MCM-41, TEOS is hydrolyzed under alkaline conditions to produce oligomeric silicate anions. Silicate anions (I^-) interact with a cationic surfactant (S^+) through electrostatic coulomb force, causing inorganic silicon species to polymerize and crosslink in the interface region. It changes the charge density of the inorganic layer, makes the long chain of the surfactant close to each other, and finally gets the orderly mesoscopic structure with the tightest accumulation of energy (S^+I^- action). Microwave enhances the Brownian motion and rotational dynamics of water molecules. In the case of rotational motion, more hydrogen bonds of water molecules are broken, producing active water molecules. Since the lone pair electrons and OH groups of the active water molecules can prevent the gel binding, the active water molecules have a higher ability to dissolve the gel [36]. Therefore, microwave

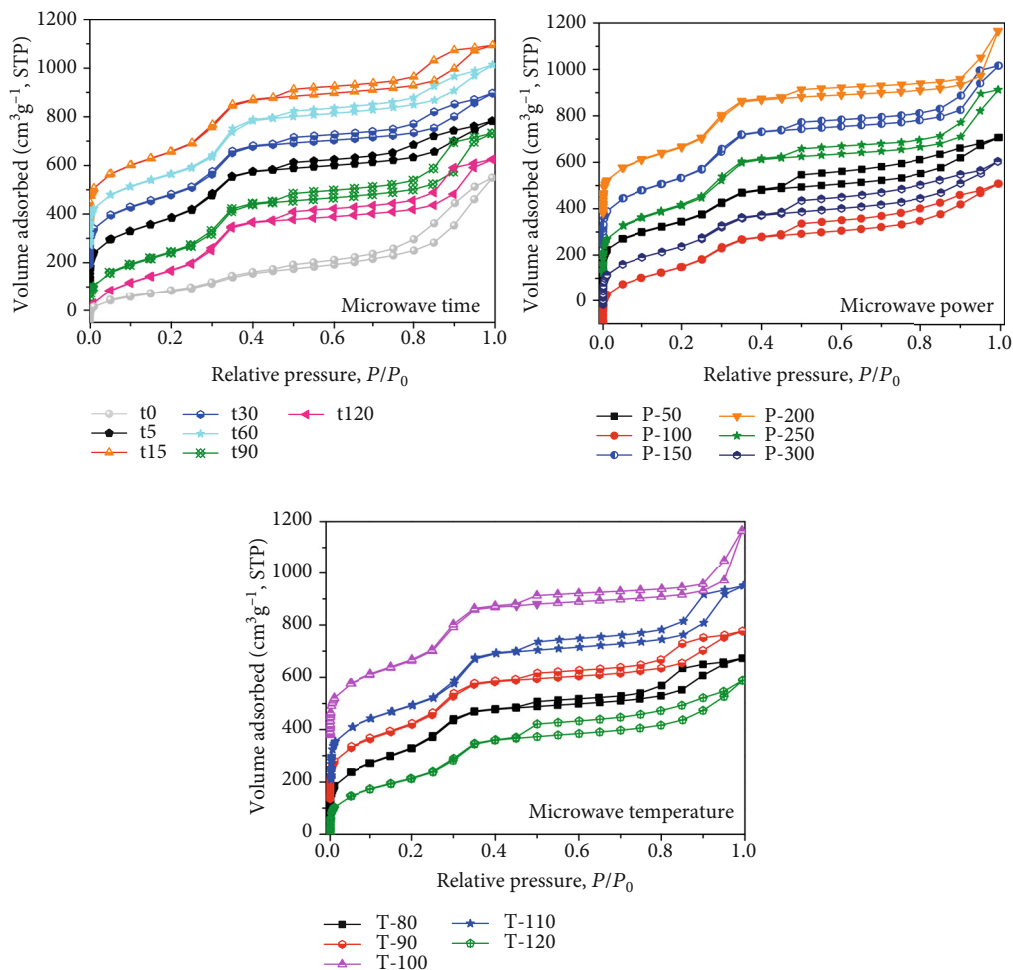


FIGURE 4: N_2 adsorption-desorption isotherms of samples obtained under different microwave conditions.

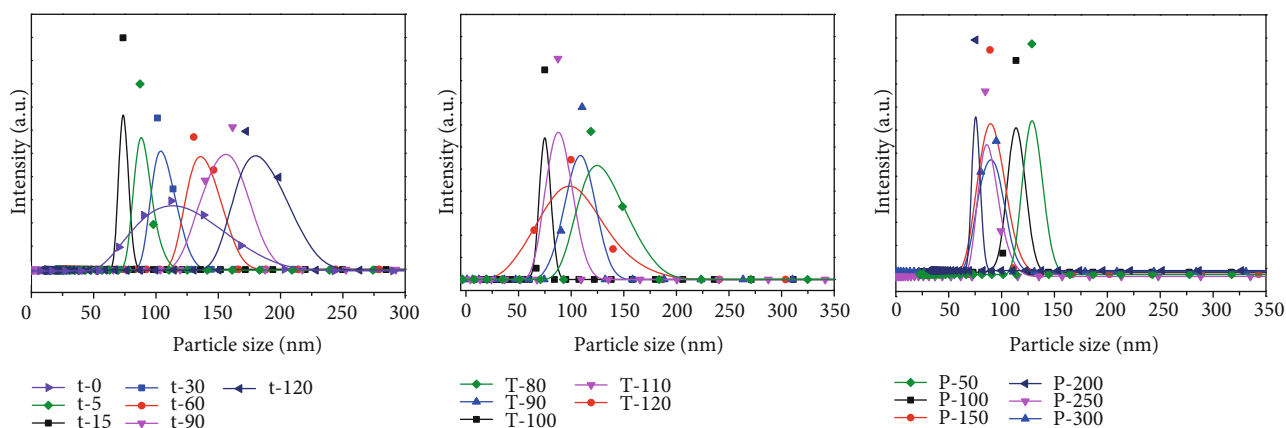


FIGURE 5: The particle size distribution of samples at different microwave conditions.

can promote the dissolution and recrystallization of the precursor and accelerate the crystallization rate. It results in rapid uniform nucleation.

3.2. Characterization of PEI-MCM-41. The FTIR spectrum of uncalcined MCM-41 and PEI-MCM-41 is shown in Figure 8.

The broad absorption band observed at $3765\text{--}3355\text{ cm}^{-1}$ was caused by the stretching of the framework Si-OH group and physically adsorbed water molecules (Figure 8(a)). Several absorption bands were observed at around $1030\text{--}1240\text{ cm}^{-1}$ in all samples which can be assigned to the Si-O-Si stretching. Uncalcined MCM-41 sample contained bands

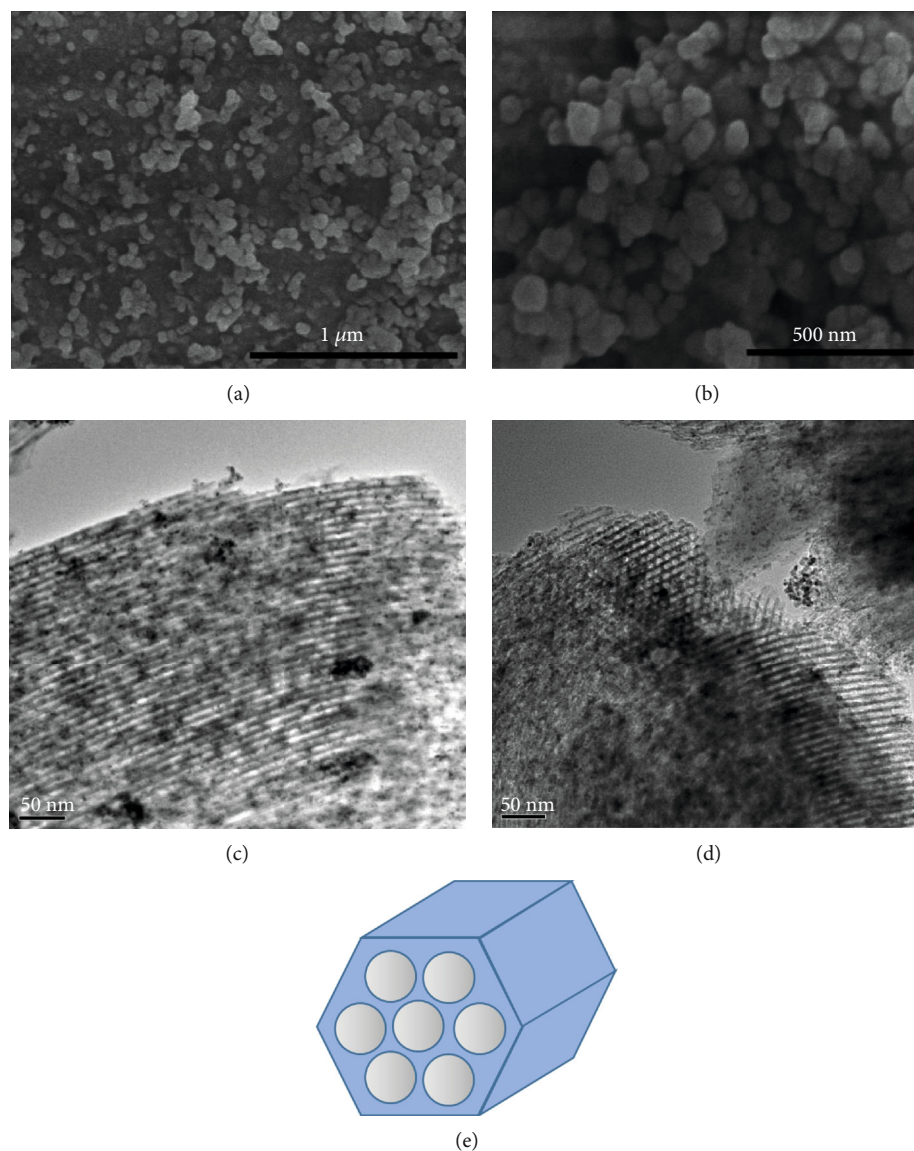


FIGURE 6: SEM (a, b) and TEM images (c, d) of WH-T100 sample. (e) Schematic diagram of the basic structure of the two-dimensional hexagonal MCM-41.

at 2850 cm^{-1} and 2930 cm^{-1} which are assigned to the C-H stretching [30]. After modification, the bands became stronger at 2850 cm^{-1} and 2930 cm^{-1} corresponding to the methyl C-H bond. The features at 1468 cm^{-1} and $1553\text{--}1646\text{ cm}^{-1}$ could be divided into -NH_2 bending and symmetric bending of NH_3^+ in the silica samples doping by PEI [37].

As can be seen from the comparison of N_2 adsorption-desorption isotherms (Figure 9(a)), since the impregnating agent occupied a large amount of pore space, S_{BET} and V of PEI-MCM-41 sharply reduced. Figure 9(b) shows TG thermograms of uncalcined MCM-41 and PEI-MCM-41. The first weight loss peak appeared at 100°C corresponding to the physically adsorbed water and CO_2 in the air. In the second stage, the weight loss of uncalcined MCM-41 was 39.78%, which was caused by the decomposition of the surfactant. For MCM-41, 63.43% weight loss of the second stage was attributed to the decomposition of surfactant and

impregnating agent. This indicated that the actual PEI load was 23.65%.

3.3. CO_2 Absorption in Pure Water and the Nanofluids. Figure 10 shows the enhancement percentage at different PEI-MCM-41 and uncalcined MCM-41 solid loading. The results implied that CO_2 capture increased as the solid loading increased, and it showed a downward trend beyond 0.1 wt%. Namely, the optimum solid loading exists for the CO_2 capture enhancement. In lower nanoparticle concentrations, increasing solid loading can promote the microconvection in liquid and give higher amounts of available sites for reacting with CO_2 , which is conducive to mass transfer. However, too dense particles are prone to problems such as particle agglomeration and uneven dispersion, resulting in a decline in the Brownian motion. It hinders the interaction between particles and decreases the mass diffusion, leading

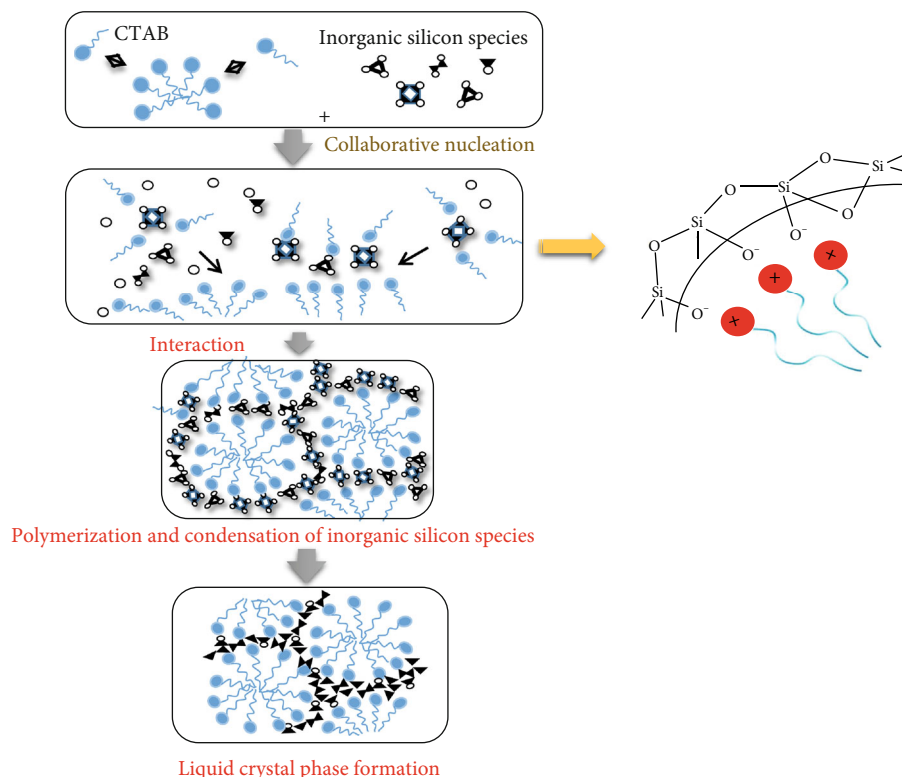


FIGURE 7: Schematic diagram of cooperative formation mechanism.

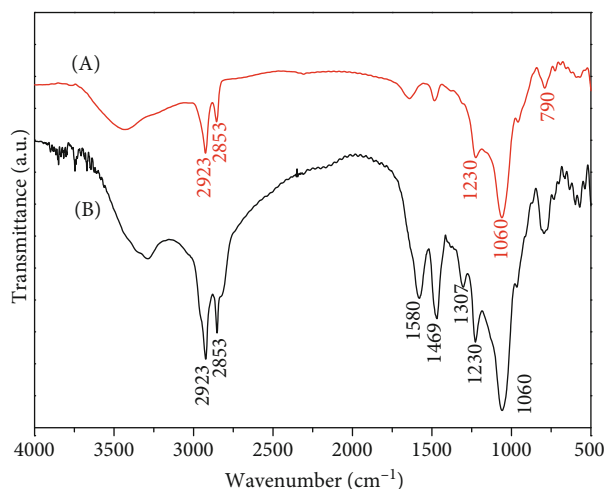


FIGURE 8: FTIR spectra of (a) uncalcined MCM-41 and (b) PEI-MCM-41.

to a negative effect on CO_2 capture. It was in agreement with Arshadi et al.'s result [38]. Based on these findings, we used 0.1 wt% as the optimal solid loading.

High-stable nanofluids can form high surface charge densities to provide sufficient repulsive forces. Zeta potential was utilized to quantify the stability of colloid dispersion. It is widely accepted that nanofluids with a zeta potential (positive or negative) more than 25 mV are phys-

ically stable [39]. The results of zeta potential of the two types of synthesized nanofluids are shown in Figure 11. The absolute values of -41.7 mV and -41.1 mV were relatively high, which demonstrated the stable nanofluids.

Figure 12(a) shows the absorption efficiency of CO_2 capture with time for pure water and nanoparticle suspensions of 0.1 wt% uncalcined MCM-41 and PEI-MCM-41. The temperature was kept constant at room temperature during all experiments. Adding nanoparticles to the water markedly raised the adsorption capacity of the fluid system towards CO_2 . The porous structure MCM-41 has an open structure and large specific surface area, with strong adsorption capacity. At the same update frequency, MCM-41 has higher mass transfer to CO_2 [40]. As seen in Figure 12(c), the water/air contact angles of uncalcined MCM-41 and PEI-MCM-41 were 32° and 53° , respectively. When the contact angle is less than 90° , the solid is hydrophilic, and the smaller the contact angle, the stronger the hydrophilicity [41]. Therefore, the two types of nanoparticles were all hydrophilic. However, when modified with PEI, the surface hydrophilicity of the MCM-41 decreased. In the case of low particle concentration, low hydrophilicity was beneficial to the adsorption of solute by providing more opportunities for particles to be in contact with CO_2 . Moreover, PEI-MCM-41 has more active sites that may react with CO_2 and larger gas absorption capacity. It not only improves the CO_2 diffusion rate but also enhances the adsorption capacity. The CO_2 absorption improvement of PEI-MCM-41/ H_2O was 25.35% higher than that of water (Figure 12(b)).

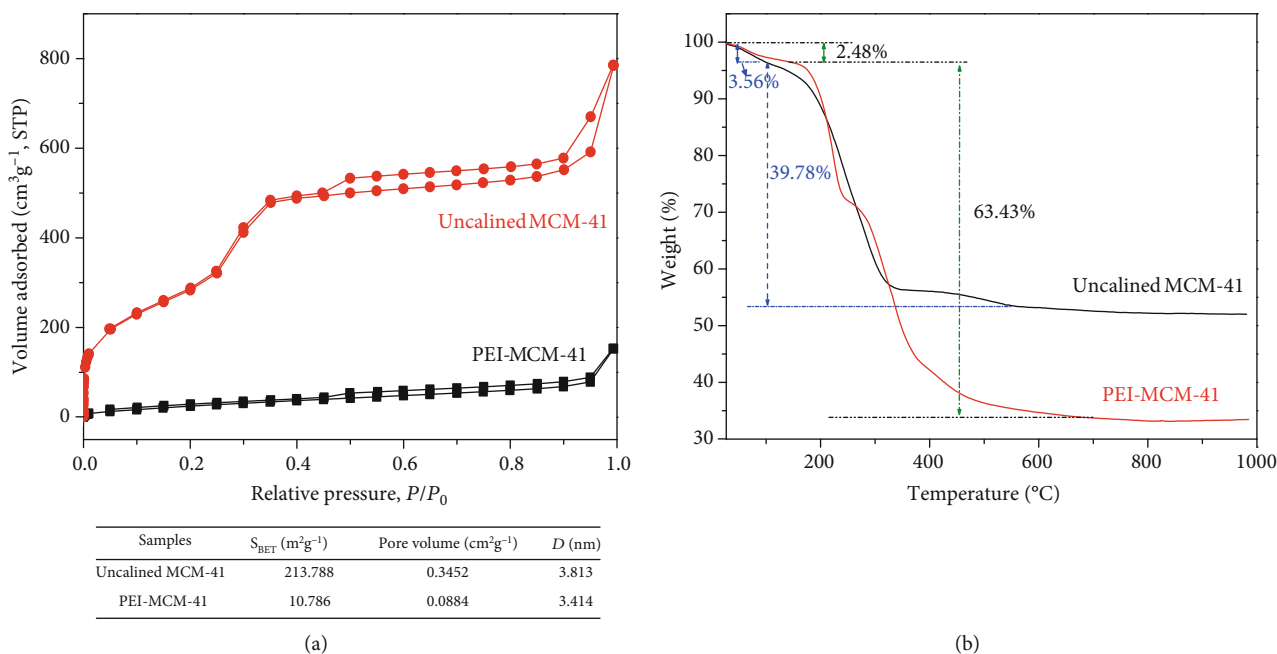


FIGURE 9: N_2 adsorption-desorption isotherms (a) and TG thermograms (b) of samples.

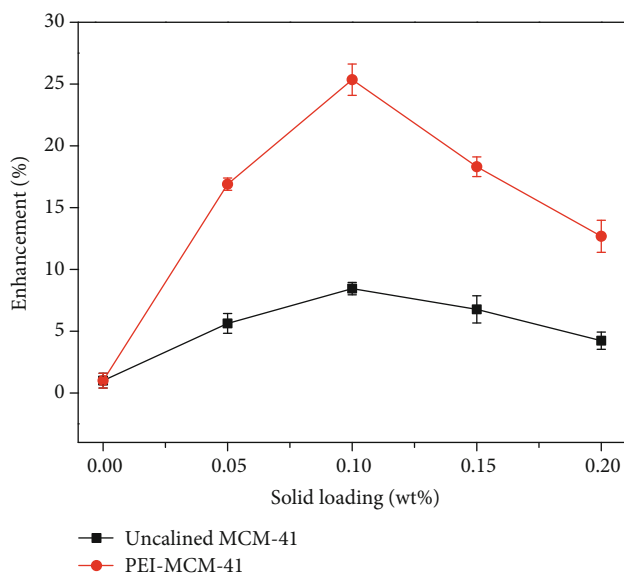


FIGURE 10: Variations in the CO_2 absorption enhancement percentage with the solid loading.

The specific enhancement mechanism is still unclear, but on the basis of previous studies, this paper summarized the possible mechanisms of absorption performance enhancement (Figure 13). Figure 13(a) shows the absorption mechanism of hydrodynamic effect, which is also called the boundary layer mixing mechanism. The presence of nanoparticles changes the hydrodynamic properties of the surrounding fluid. The nanoparticles collide at the gas-liquid interface inducing local turbulence, reducing the thickness of the mass transfer membrane and refreshing the gas-liquid boundary layer. Figure 13(b) shows the

absorption mechanism of grazing effect, which is called the transmission mechanism. Since the size of nanoparticles is smaller than the thickness of the mass transfer membrane, the nanoparticles can penetrate the membrane and transport a certain amount of gas into the liquid bulk. Figure 13(c) shows the absorption mechanism of preventing bubble coalescence which states that the nanoparticles can easily adhere to the bubble surface. Due to the addition of nanoparticles, the movement of liquid becomes more dynamic. The collision between the nanoparticles and the gas-liquid interface caused the bubbles to be broken into small bubbles. Furthermore, nanoparticles strengthen bubble stiffness, reduce bubble coalescence speed, and increase the gas-liquid interface area. The mass transfer process in the bubbling reactor is accompanied by the bubble rising and growing, which undergoes a constantly changing gas-liquid interface area. During the CO_2 bubble absorption process, uncalined MCM-41 or PEI-MCM-41 collide with the gas-liquid interface and each other under the action of Brownian motion, breaking up bubbles in the fluid into smaller bubbles [38]. At the same time, nanoparticles adhere to the surface of bubbles, reducing bubble collision and the rate of bubble coalescence. These two behaviors effectively increase the phase interface area, reduce the mass transfer resistance, and promote the diffusion of CO_2 into the water. In addition, the presence of particles increases the degree of microdisturbance and turbulence of the boundary layer; these results in redistribution of the liquid film, acceleration of the liquid film surface renewal rate, and the exchange of substances in the membrane [42]. The mass transfer effect is enhanced to some extent. Even if the particle concentration is small, the flow fields around the nanoparticles also interact. Furthermore, PEI-MCM-41 as a promoter features amine functional sites that can chemically interact with CO_2 and exhibits the higher gas absorption.

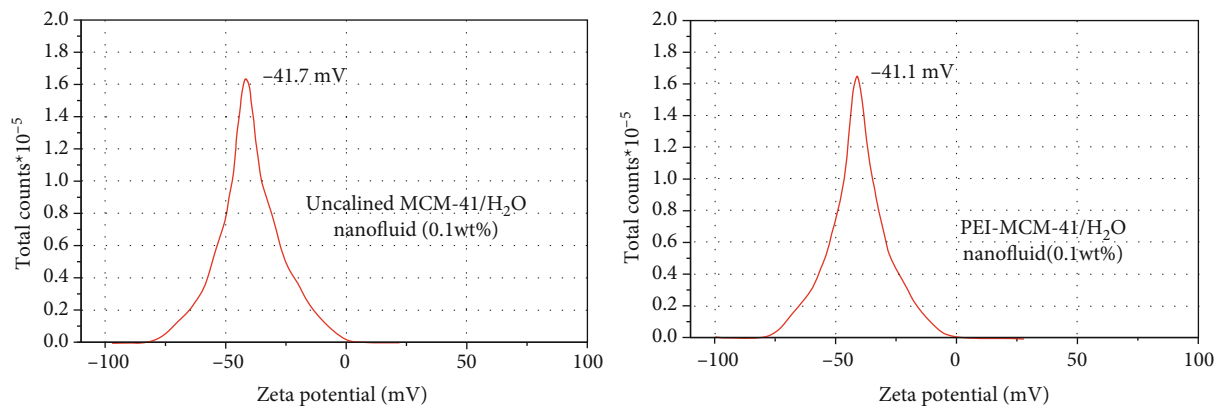
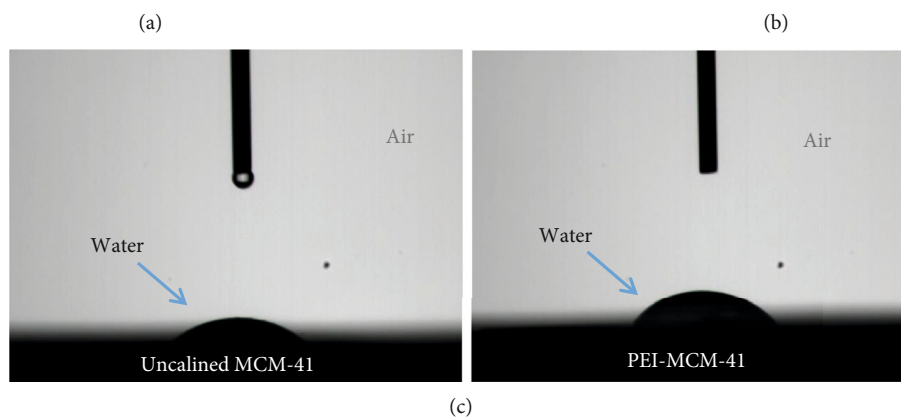
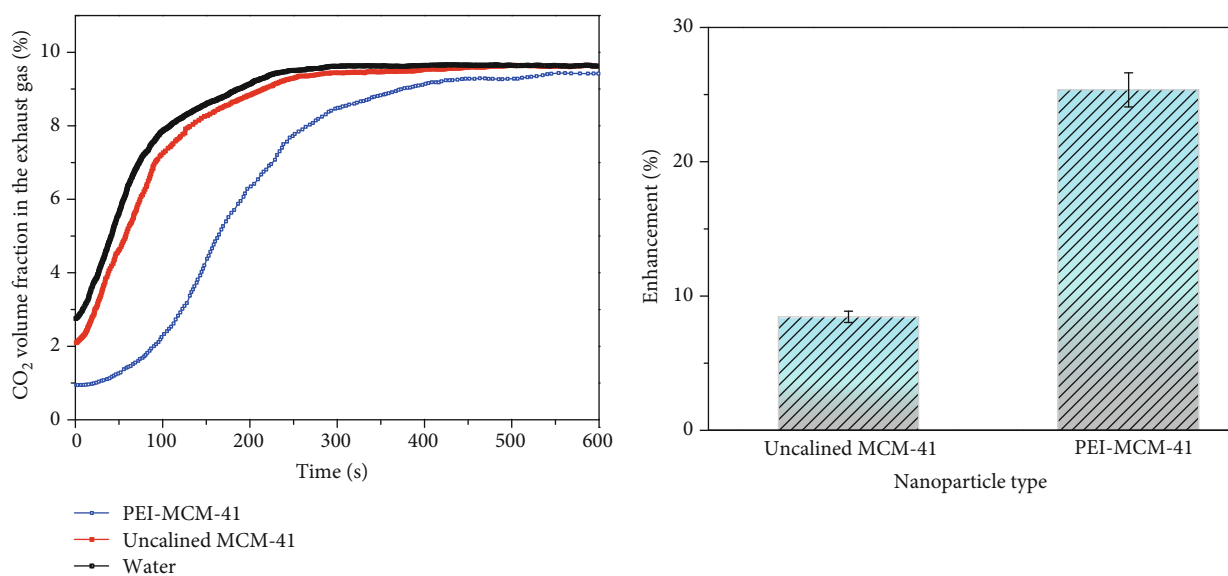


FIGURE 11: The zeta potential of the synthesized nanofluids.



(c)

FIGURE 12: (a) Output CO₂ concentration as a function of time, (b) CO₂ absorption improvement of various nanoparticles in water, and (c) water wettability of the prepared nanoparticles in air.

4. Conclusion

In summary, an ordered mesoporous silica material MCM-41 was synthesized by microwave technology. Microwave can promote the dissolution and recrystallization of the precursor and accelerate the crystallization rate. The effects

of different microwave conditions on MCM-41 were elucidated minutely in this paper. The optimum conditions for preparation of MCM-41 were the microwave time of 15 min, microwave temperature of 100°C, and microwave power of 200 W. Under this condition, MCM-41 with narrow particle size distribution, average diameter of 50 nm, and

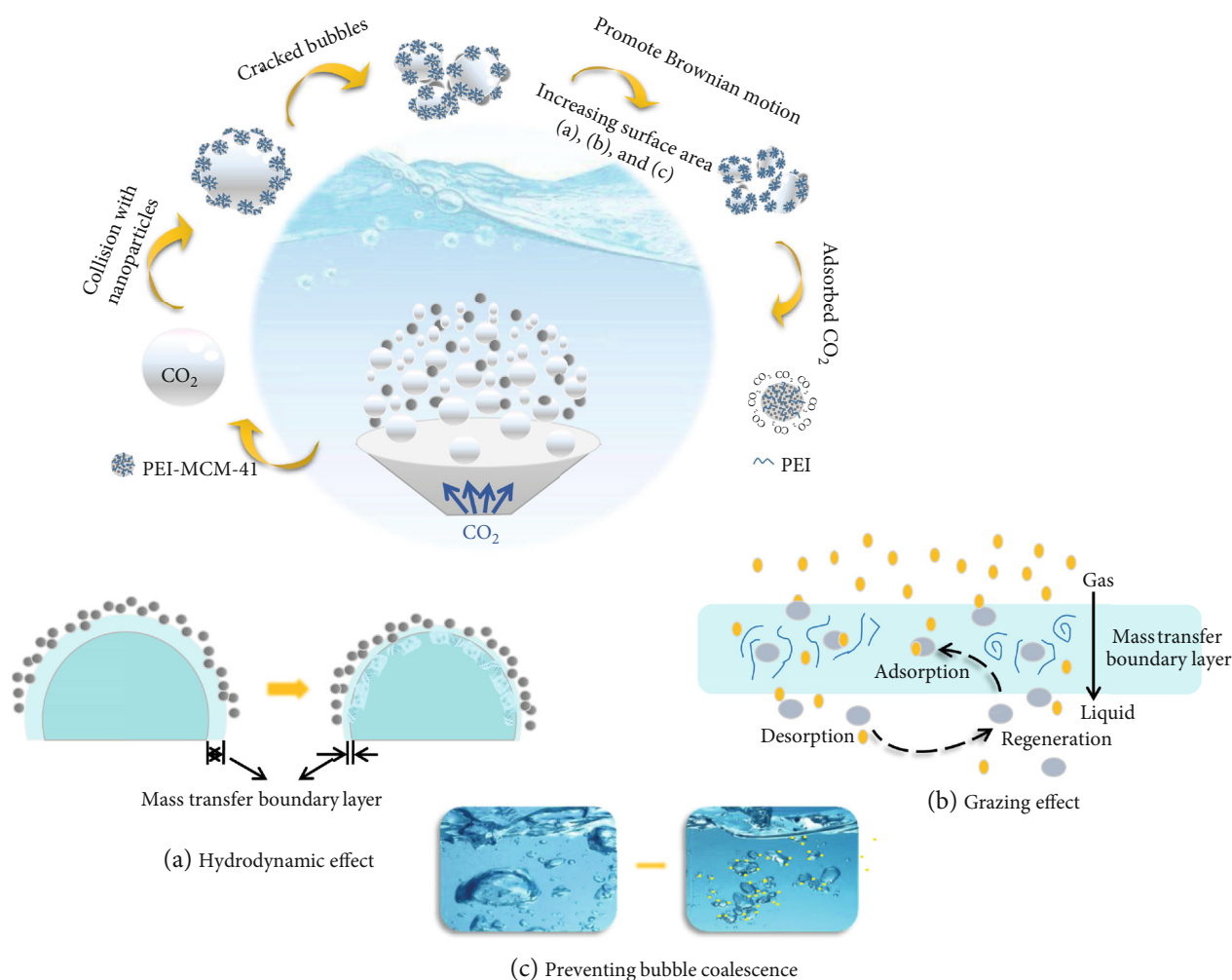


FIGURE 13: Schematic diagram of absorption mechanisms.

S_{BET} of $1210.3 \text{ m}^2 \text{ g}^{-1}$ was obtained. Furthermore, the CO₂ absorption performance in water-based nanofluids in the presence of two types of nanoparticles of uncalcined MCM-41 and PEI-MCM-41 was evaluated. The enhancement effect of PEI-MCM-41 nanoparticles was more obvious than that of uncalcined MCM-41. The CO₂ absorption improvement of uncalcined MCM-41 (0.1 wt%)/H₂O was 8.45% higher than that of water. PEI-MCM-41 as a promoter not only increased the CO₂ diffusion rate but also enhanced the adsorption capacity due to the fact that it owns more active sites that may react with CO₂. The CO₂ absorption improvement of PEI-MCM-41 (0.1 wt%)/H₂O was 25.35% higher than that of water. MCM-41 has a potential to enhance the mass transfer both before and after modification. However, in the future work, it is necessary to further study the influence of modifier type on absorption effect and the regeneration performance of nanofluid systems.

Data Availability

The data used to support the findings of this study are included within the article.

Conflicts of Interest

There are no conflicts to declare.

Acknowledgments

The authors wish to express their thanks for the financial support from the Shanxi Graduate Education Innovation Program (2019BY060) and the 16th Graduate Technology Project of North University of China (20191623).

References

- [1] G. Haddow, J. A. Bullock, and K. Haddow, *Global warming, natural hazards, and emergency management*, Routledge, 2017.
- [2] R. K. Pachauri and A. Reisinger, *Climate change 2014: synthesis report. Contribution of Working Groups I, II and III to the fifth assessment report of the Intergovernmental Panel on Climate Change*, IPCC, 2014.
- [3] F. Song and Z. H. Liu, "Global carbon emissions hit a new high in 2018," *Ecological Economy*, vol. 35, no. 2, pp. 5–8, 2019.
- [4] P. Markewitz, W. Kuckshinrichs, W. Leitner et al., "Worldwide innovations in the development of carbon capture

- technologies and the utilization of CO₂,” *Energy & Environmental Science*, vol. 5, no. 6, pp. 7281–7305, 2012.
- [5] A. A. Olajire, “CO₂ capture and separation technologies for end-of-pipe applications – A review,” *Energy*, vol. 35, no. 6, pp. 2610–2628, 2010.
 - [6] H. Yang, Z. Xu, M. Fan et al., “Progress in carbon dioxide separation and capture: a review,” *Journal of Environmental Sciences*, vol. 20, no. 1, pp. 14–27, 2008.
 - [7] H. Machida, K. Oba, T. Tomikawa, T. Esaki, T. Yamaguchi, and H. Horizoe, “Development of phase separation solvent for CO₂ capture by aqueous (amine + ether) solution,” *The Journal of Chemical Thermodynamics*, vol. 113, pp. 64–70, 2017.
 - [8] R. Feng, X. Hu, Y. Ma et al., “Synthesis of poly (styrene-divinylbenzene) by nano-TiO₂ and the application for pipette-tip solid-phase extraction of flavonoid in *Epipremnum aureum* rhizome,” *Separation Science and Technology*, pp. 1–9, 2019.
 - [9] Z. Ziobrowski, R. Krupiczka, and A. Rotkegel, “Carbon dioxide absorption in a packed column using imidazolium based ionic liquids and MEA solution,” *International Journal of Greenhouse Gas Control*, vol. 47, pp. 8–16, 2016.
 - [10] M. Mendt, B. Jee, D. Himsl et al., “A continuous-wave electron paramagnetic resonance study of carbon dioxide adsorption on the metal–organic frame-work MIL-53,” *Applied Magnetic Resonance*, vol. 45, no. 3, pp. 269–285, 2014.
 - [11] L. Nie, Y. Mu, J. Jin, J. Chen, and J. Mi, “Recent developments and consideration issues in solid adsorbents for CO₂ capture from flue gas,” *Chinese Journal of Chemical Engineering*, vol. 26, no. 11, pp. 2303–2317, 2018.
 - [12] Q. Liu, J. Shi, S. Zheng, M. Tao, Y. He, and Y. Shi, “Kinetics studies of CO₂ Adsorption/Desorption on amine-functionalized multiwalled carbon nanotubes,” *Industrial & Engineering Chemistry Research*, vol. 53, no. 29, pp. 11677–11683, 2014.
 - [13] C. Song, Q. Liu, N. Ji, S. Deng, J. Zhao, and Y. Kitamura, “Advanced cryogenic CO₂ capture process based on Stirling coolers by heat integration,” *Applied Thermal Engineering*, vol. 114, pp. 887–895, 2017.
 - [14] C. F. Song, Y. Kitamura, S. H. Li, and W. Z. Jiang, “Analysis of CO₂ frost formation properties in cryogenic capture process,” *International Journal of Greenhouse Gas Control*, vol. 13, pp. 26–33, 2013.
 - [15] A. M. Yousef, W. M. el-Maghlany, Y. A. Eldrainy, and A. Attia, “New approach for biogas purification using cryogenic separation and distillation process for CO₂ capture,” *Energy*, vol. 156, pp. 328–351, 2018.
 - [16] A. D. Ebner and J. A. Ritter, “State-of-the-art adsorption and membrane separation processes for carbon dioxide production from carbon dioxide emitting industries,” *Separation Science and Technology*, vol. 44, no. 6, pp. 1273–1421, 2009.
 - [17] A. Brunetti, E. Drioli, Y. M. Lee, and G. Barbieri, “Engineering evaluation of CO₂ separation by membrane gas separation systems,” *Journal of Membrane Science*, vol. 454, pp. 305–315, 2014.
 - [18] Z. Y. Yeo, T. L. Chew, P. W. Zhu, A. R. Mohamed, and S. P. Chai, “Synthesis and performance of microporous inorganic membranes for CO₂ separation: a review,” *Journal of Porous Materials*, vol. 20, no. 6, pp. 1457–1475, 2013.
 - [19] S.-S. Ashrafmansouri and M. Nasr Esfahany, “Mass transfer in nanofluids: a review,” *International Journal of Thermal Sciences*, vol. 82, pp. 84–99, 2014.
 - [20] H. Beiki, M. N. Esfahany, and N. Etesami, “Turbulent mass transfer of Al₂O₃ and TiO₂ electrolyte nanofluids in circular tube,” *Microfluidics and Nanofluidics*, vol. 15, no. 4, pp. 501–508, 2013.
 - [21] N. Keshishian, M. Nasr Esfahany, and N. Etesami, “Experimental investigation of mass transfer of active ions in silica nanofluids,” *International Communications in Heat and Mass Transfer*, vol. 46, pp. 148–153, 2013.
 - [22] W. Li, C. Zou, and X. Li, “Thermo-physical properties of cooling water-based nanofluids containing TiO₂ nanoparticles modified by Ag elementary substance for crystallizer cooling system,” *Powder Technology*, vol. 329, pp. 434–444, 2018.
 - [23] W. Li and C. Zou, “Experimental investigation of stability and thermo-physical properties of functionalized β-CD-TiO₂-Ag nanofluids for antifreeze,” *Powder Technology*, vol. 340, pp. 290–298, 2018.
 - [24] W. Li and C. Zou, “Deep desulfurization of gasoline by synergistic effect of functionalized β-CD-TiO₂-Ag nanoparticles with ionic liquid,” *Fuel*, vol. 227, pp. 141–149, 2018.
 - [25] M. P. Mokhonoana and N. J. Coville, “Synthesis of [Si]-MCM-41 from TEOS and water glass: the water glass-enhanced condensation of TEOS under alkaline conditions,” *Journal of Sol-Gel Science and Technology*, vol. 54, no. 1, pp. 83–92, 2010.
 - [26] H. Misran, R. Singh, S. Begum, and M. A. Yarmo, “Processing of mesoporous silica materials (MCM-41) from coal fly ash,” *Journal of Materials Processing Technology*, vol. 186, no. 1–3, pp. 8–13, 2007.
 - [27] T. Heikkilä, H. A. Santos, N. Kumar et al., “Cytotoxicity study of ordered mesoporous silica MCM-41 and SBA-15 microparticles on Caco-2 cells,” *European Journal of Pharmaceutics and Biopharmaceutics*, vol. 74, no. 3, pp. 483–494, 2010.
 - [28] P. Fu, T. Yang, J. Feng, and H. Yang, “Synthesis of mesoporous silica MCM-41 using sodium silicate derived from copper ore tailings with an alkaline molted-salt method,” *Journal of Industrial and Engineering Chemistry*, vol. 29, pp. 338–343, 2015.
 - [29] N. H. N. Kamarudin, A. A. Jalil, S. Triwahyono et al., “Variation of the crystal growth of mesoporous silica nanoparticles and the evaluation to ibuprofen loading and release,” *Journal of Colloid and Interface Science*, vol. 421, pp. 6–13, 2014.
 - [30] A. N. Ergün, Z. Ö. Kocabaş, M. Baysal, A. Yürüm, and Y. Yürüm, “Synthesis of mesoporous MCM-41 materials with low-power microwave heating,” *Chemical Engineering Communications*, vol. 200, no. 8, pp. 1057–1070, 2013.
 - [31] P. M. Carraro, A. A. G. Blanco, F. A. Soria et al., “Understanding the role of nickel on the hydrogen storage capacity of Ni/MCM-41 materials,” *Microporous and Mesoporous Materials*, vol. 231, pp. 31–39, 2016.
 - [32] V. B. Felonov, V. N. Romannikov, and A. Y. Derevyankin, “Mesopore size and surface area calculations for hexagonal mesophases (types MCM-41, FSM-16, etc.) using low-angle XRD and adsorption data,” *Microporous and Mesoporous Materials*, vol. 28, no. 1, pp. 57–72, 1999.
 - [33] M. Thommes, K. Kaneko, A. V. Neimark et al., “Physisorption of gases, with special reference to the evaluation of surface area and pore size distribution (IUPAC Technical Report),” *Pure and Applied Chemistry*, vol. 87, no. 9–10, pp. 1051–1069, 2015.
 - [34] T. Wang, H. Kaper, M. Antonietti, and B. Smarsly, “Templating behavior of a long-chain ionic liquid in the hydrothermal

- synthesis of mesoporous silica,” *Langmuir*, vol. 23, no. 3, pp. 1489–1495, 2007.
- [35] H. L. Fan, S. F. Zhou, G. S. Qi, and Y. Z. Liu, “Continuous preparation of Fe_3O_4 nanoparticles using impinging stream-rotating packed bed reactor and magnetic property thereof,” *Journal of Alloys and Compounds*, vol. 662, pp. 497–504, 2016.
- [36] W. C. Conner, G. Tompsett, K. H. Lee, and K. S. Yngvesson, “Microwave synthesis of zeolites: 1. Reactor engineering,” *The Journal of Physical Chemistry B*, vol. 108, no. 37, pp. 13913–13920, 2004.
- [37] Q. Wang, M. Zhu, B. Dai, and J. Zhang, “A novel and effective Zn/PEI-MCM catalyst for the acetylene hydration to acetaldehyde,” *Chinese Chemical Letters*, vol. 30, no. 6, pp. 1244–1248, 2019.
- [38] M. Arshadi, H. Taghvaei, M. K. Abdolmaleki, M. Lee, H. Eskandarloo, and A. Abbaspourrad, “Carbon dioxide absorption in water/nanofluid by a symmetric amine-based nanodendritic adsorbent,” *Applied Energy*, vol. 242, pp. 1562–1572, 2019.
- [39] V. Irani, A. Tavasoli, A. Maleki, and M. Vahidi, “Polyethyleneimine-functionalized HKUST-1/MDEA nanofluid to enhance the absorption of CO_2 in gas sweetening process,” *International Journal of Hydrogen Energy*, vol. 43, no. 11, pp. 5610–5619, 2018.
- [40] S. Y. Cheng, Y. Z. Liu, and G. S. Qi, “Progress in the enhancement of gas–liquid mass transfer by porous nanoparticle nanofluids,” *Journal of Materials Science*, vol. 54, no. 20, pp. 13029–13044, 2019.
- [41] B. P. Binks and S. O. Lumsdon, “Influence of particle wettability on the type and stability of surfactant-free emulsions,” *Langmuir*, vol. 16, no. 23, pp. 8622–8631, 2000.
- [42] S. Lu, Y. Zhao, J. Song, and Y. Li, “Experimental studies of CO_2 absorption enhancement in water-based nanofluids of carbon nanotubes,” *Brazilian Journal of Chemical Engineering*, vol. 34, no. 2, pp. 597–606, 2017.